CrystEngComm

PAPER

View Article Online
View Journal | View Issue

Cite this: *CrystEngComm*, 2025, **27**, 2683

Crystal structure and magnetoresistance of vacancy-ordered perovskite $SrV_{0.3}Fe_{0.7}O_{2.8}$ at low temperature†

Teppei Nagase, [a] Takumi Nishikubo, [abc] Yuki Sakai, [ac] Kei Shigematsu, [abc] Ko Mibu, [d] Masato Hagihala, [e] Masaki Azuma [abc] and Takafumi Yamamoto *[af]

Received 8th January 2025,
Accepted 9th March 2025

DOI: 10.1039/d5ce00028a

rsc.li/crystengcomm

Vacancy-ordering in perovskite oxides brings a rich variety of structures and accompanying physical properties. Previously, we reported room-temperature magnetoresistance in $SrV_{0.3}Fe_{0.7}O_{2.8}$ with ordered oxygen vacancies in the primitive perovskite $(111)_p$ plane. In this report, we characterize the structure and physical properties of $SrV_{0.3}Fe_{0.7}O_{2.8}$ at low temperatures. This compound undergoes a structural phase transition from the rhombohedral phase to the monoclinic phase by cooling down to T_s = 200 K. The transition induces octahedral tilting, affecting its magnetization behaviour: The compound shows weak ferromagnetism with almost zero coercivity above T_s, while the coercivity prominently increases below T_s, keeping its weak ferromagnetism. We also observed an enhancement of magnetoresistance by decreasing temperature, reaching −18% at 130 K and 9 T.

Introduction

Perovskite oxides (ABO_3, A and B are cations) show fascinating properties owing to their variety of composition and derived structures. Many perovskite oxides can adopt oxygen vacancies, which modify their crystal structure and electronic state, bringing various properties.[1–3] When the oxygen vacancy level (δ in $ABO_{3-\delta}$) is commensurate with respect to the underlying lattice, the oxygen vacancies often align as typically seen in the $ABO_{2.5}$ brownmillerite structure[4,5] and ABO_2 infinite-layer structure.[6,7] Recently, several compounds with ordered oxygen vacancies in every fifth primitive perovskite $(111)_p$ plane (p represents primitive perovskite cell), the so-called "15R-structure", have been reported.[8–11] These materials show unique characteristics such as charge density wave-type ordering in $SrCrO_{2.8}$ and the quasi-two-dimensional metallic state caused by the layered structure along the $[111]_p$ direction in $SrVO_{2.2}N_{0.6}$.

In a previous report, we found a new 15R perovskite oxide $SrV_{0.3}Fe_{0.7}O_{2.8}$ (Fig. 1a).[9] In this compound, B-site cations are ordered along the $[111]_p$ direction accompanied by the ordered oxygen vacancies: the octahedral sites are occupied by 100% of Fe^{3+}, and the tetrahedral site is occupied by 25% of Fe^{3+} and 75% of V^{5+}, leading to a layered structure of a semiconducting magnetic octahedral layer and an insulating diluted magnetic tetrahedral layer with 25% of magnetic cation, $Fe^{3+}(d^5)$. This compound shows weak ferromagnetic ordering with a small saturation moment (*ca.* 0.4 μ_B/Fe atom) at room temperature. In addition, this compound exhibits large negative magnetoresistance (−5% at 9 T) at room temperature by the tunnelling mechanism.

Here, we report the crystal structure and physical properties of $SrV_{0.3}Fe_{0.7}O_{2.8}$ at low temperatures. We found that this compound undergoes a structural phase transition at 200 K, caused by octahedral tilting. We discuss the effect of the transition on the magnetic property. Furthermore, we also found enhancement of the magnetoresistance at low temperatures (−18% at 130 K and 9 T).

Experimental

$SrV_{0.3}Fe_{0.7}O_{2.8}$ was synthesized by the standard high-temperature solid-state reaction as reported previously.[9] The raw materials, $SrCO_3$, V_2O_5, and Fe_2O_3, were mixed and

[a] *Materials and Structures Laboratory, Institute of Integrated Research, Institute of Science Tokyo, Yokohama, Kanagawa 226-8501, Japan*
[b] *Research Center for Autonomous Systems Materialogy (ASMat), Institute of Integrated Research, Institute of Science Tokyo, 4259 Nagatsuta-cho, Midori-ku, Yokohama, Kanagawa, 226-8501, Japan*
[c] *Kanagawa Institute of Industrial Science and Technology, 705–1 Shimoimaizumi, Ebina 243-0435, Japan*
[d] *Department of Physical Science and Engineering, Nagoya Institute of Technology, Nagoya 466-8555, Japan*
[e] *Neutron Science Division, Institute of Materials Structure Science, High Energy Accelerator Research Organization, Tsukuba, Japan*
[f] *Department of Chemistry, Graduate School of Science, Kyoto University, Kitashirakawa Oiwake-cho, Sakyoku, Kyoto, 606-8502, Japan.*
E-mail: yama@kuchem.kyoto-u.ac.jp

† Electronic supplementary information (ESI) available. See DOI: https://doi.org/10.1039/d5ce00028a

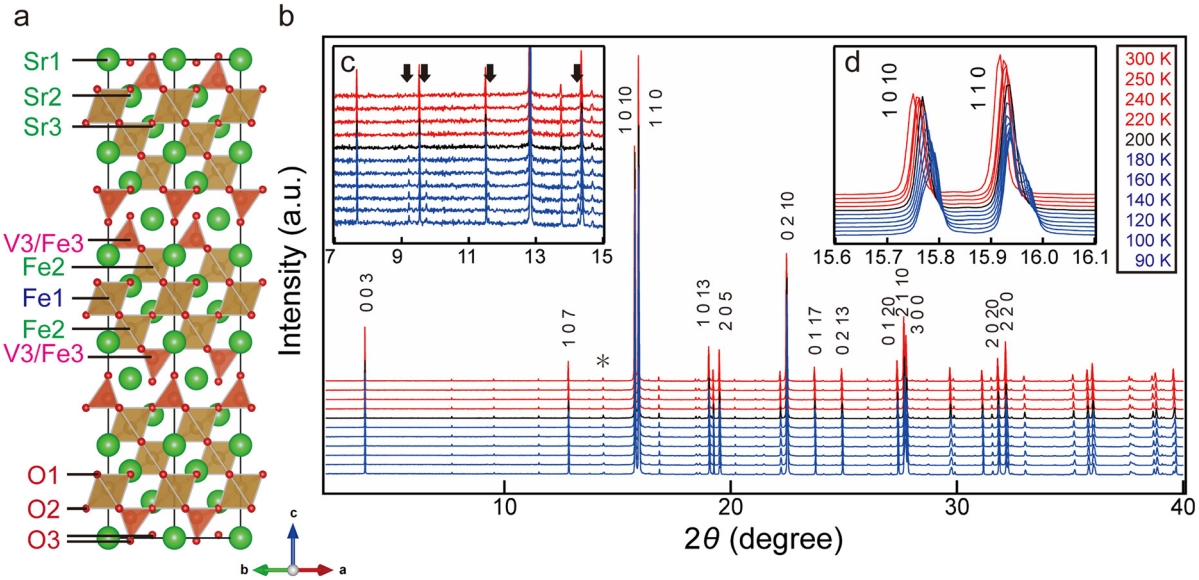

Fig. 1 (a) Ideal crystal structure of $SrV_{0.3}Fe_{0.7}O_{2.8}$ at room temperature. The displacement disorders of Sr1 and O3 sites are simplified in Fig. 1a. (b) Synchrotron XRD patterns for $SrVe_{0.3}Fe_{0.7}O_{2.8}$. The asterisk * in Fig. 1b shows the impurity $Sr_3V_2O_8$. Expansions of synchrotron XRD patterns are shown in the inset figures (c) and (d). The arrows in Fig. 1c denote the peak positions originating from the low-temperature phase. The detailed peak indexes are shown in Fig. S2.† Crystal structures are visualized with VESTA 3.[12]

ground with acetone. The obtained dry powder was pelletized and calcined at 1000 °C for 1 h in air. The calcined sample was crushed and ground. The obtained powder was pelletized again and sintered at 1150 °C for 72 h in air with two intermediate grindings.

The detailed structure at low temperatures was investigated by using high-resolution synchrotron X-ray diffraction (XRD) measurements to detect the peak splitting and negligibly small peaks. The synchrotron XRD data were collected at the beamline BL02B2 (JASRI, SPring-8). The incident beam from a bending magnet was monochromatized to 0.77407 Å. The ground powder sample (particle size is about 1–10 μm; see Fig. S1†) was put into a quartz capillary of 0.2 mm in outer diameter. The sealed capillary was cooled with a low temperature N_2 gas flow device and rotated during measurements to reduce the effect of potential preferential orientation. We carried out temperature dependence of neutron diffraction (ND) below room temperature on a high-resolution time-of-flight powder diffractometer SuperHRPD in the Materials and Life Science Experimental Facility (MLF) of the Japan Proton Accelerator Research Complex (J-PARC). The obtained synchrotron XRD and ND data were analyzed using Jana2006.[13]

Mössbauer spectra for $SrV_{0.3}Fe_{0.7}O_{2.8}$ were taken at 78 K, 200 K, and 300 K in a conventional transmission geometry using a ^{57}Co/Rh γ-ray source. The source velocity was calibrated by α-Fe as a reference material.

Magnetic susceptibility was measured by using a SQUID magnetometer (MPMS, Quantum Design, Inc.). Electric resistance was recorded in the range of 130–300 K by a two-probe method in PPMS with an externally equipped source (Keithley 2450 SMU, Tektronix Inc.). The magnetic field was applied using PPMS. The magnetoresistance MR is calculated using the following equation.

$$\mathrm{MR}(H,\ T) = \frac{R(H,\ T) - R(0\mathrm{T},\ \mathrm{T})}{R(0\mathrm{T},\ \mathrm{T})} \quad (1)$$

Here, $R(H, T)$ represents the resistance at H [T] and T [K].

Results and discussion

Fig. 1b–d show the temperature dependence of the synchrotron XRD pattern for $SrV_{0.3}Fe_{0.7}O_{2.8}$. At room temperature, the pattern could be indexed on a rhombohedral cell ($R\bar{3}m$) with a = 5.59349(1) Å and c = 34.7975(1) Å, consistent with the previous report.[9] When the temperature decreases, the peaks gradually shift to higher angles. In addition, small peaks appear below 200 K (arrows in Fig. 1c). Simultaneously, the splitting of the main peaks (1 1 0 and 1 0 10) was observed (Fig. 1d), indicating the occurrence of the structural phase transition (T_s = 200 K). The peak splitting occurs gradually, indicating a second-order phase transition. Among the maximal non-isomorphic subgroups of $R\bar{3}m$ (I: $R3m$, $R32$, $R\bar{3}1$, and $C2/m$; IIa: $P\bar{3}m1$, and IIb: $R\bar{3}m$, and $R\bar{3}c$), $C2/m$ is a plausible space group for the low-temperature phase since it can only allow the peak splitting of the main peaks (1 1 0 and 1 0 10). We screened the superstructure by using ISODISTORT.[14] Considering the peak positions of the synchrotron XRD pattern, we selected space groups $C2/m$ or $C2/c$ with a = 9.68 Å, b = 5.59 Å, c = 23.39 Å, and β = 97.93°, which are transformed from the original rhombohedral cell by the following matrix (Fig. 3a and b).

$$(a_M b_M c_M) = (a_R b_R c_R)\begin{pmatrix} 1 & -1 & -\frac{1}{3} \\ -1 & -1 & \frac{1}{3} \\ 0 & 0 & -\frac{2}{3} \end{pmatrix} \quad (2)$$

Here, the two space groups are the klassengleiche subgroups of $C2/m$, which is the translationengleiche subgroup of the room temperature phase. By using this cell size, all the peaks at 90 K can be fitted by Le Bail analysis. $C2/c$ has a c glide plane and shows fewer reflections than $C2/m$ by the reflection conditions ($h0l$: l is odd). Since these reflections are absent in the experimental data (Fig. S3†), $C2/c$ is chosen. The obtained lattice parameters are a = 9.68235(3) Å, b = 5.57301(2) Å, c = 23.3663(1) Å, and β = 97.8936(3)°.

Fig. 2 shows the temperature dependence of lattice parameters a_R and c_R for the high-temperature rhombohedral phase and b_M, normalized a_M $\left(\frac{1}{\sqrt{3}}a_M\right)$ and normalized c_M $\left(\frac{3}{2}c_M \sin\beta_M\right)$ for the low-temperature monoclinic phase. Here, subscripted M and R denote monoclinic and rhombohedral cells, respectively. The changes from a_R to normalized a_M and b_M and from c_R to normalized c_M are continuous, confirming the second-order phase transition. Although c_R and c_M decrease monotonously, a_R splits into a_M and b_M below T_s. a_M and b_M are longer and shorter, respectively, than a_{ave} by 0.1–0.2%.

There are several structures that can be considered as a member of the (111) vacancy-ordered perovskite $A_nB^{oct}{}_{n-2}B^{tet}{}_2O_{3n-1}$ (B^{oct} and B^{tet} represent cations in octahedral and tetrahedral sites, respectively).[8–11,15,16] Glaserite-type oxides $Na_2BaMV_2O_8$ (M = Mn, Fe, and $Mn_{0.6}Co_{0.4}$),[17–19] which are examples of that member, show a second order phase transition with the symmetry reduction (from $P\bar{3}m1$ to $C2/c$) at low temperature. The primary origin of the phase transition was reported as polyhedral tilting (Fig. 3d).[17] Considering the similarities of the structure and symmetry reduction between $SrV_{0.3}Fe_{0.7}O_{2.8}$ and $Na_2BaMV_2O_8$, the primary origin of the phase transition in $SrV_{0.3}Fe_{0.7}O_{2.8}$ is also considered as polyhedral tilting.

To prove the octahedral tilting, we performed Rietveld analysis of synchrotron X-ray and neutron powder diffraction data to precisely determine the atomic positions. We refined atomic positions of oxygen with those of cations fixed in the analysis of neutron diffraction data. The obtained neutron diffraction pattern contains some magnetic reflections. The magnetic structure of $SrV_{0.3}Fe_{0.7}O_{2.8}$ consists of the G-type antiferromagnetic component with the propagation vector $\mathbf{k}$ = (0, 0, 3/2) and ferromagnetic component with $\mathbf{k}$ = (0, 0, 0) at room temperature.[9] The result of refinement, including the magnetic structure, is shown in Fig. S4 and Table S1.† Although it is difficult to determine the precious oxygen positions due to the overlapped magnetic reflections, the combination of polyhedral rotation along the a_M-axis and c^*_M-axis is observed as illustrated in Fig. S5,† which is the same to Glaserite-type oxides. Considering the symmetry reduction and the change of the lattice parameters, the rotation along the a_M-axis is dominant. Therefore, this structural phase transition is caused by the polyhedral rotation along mainly the a_M-axis (Fig. 3c).

In order to obtain further information about the transition, we carried out ^{57}Fe Mössbauer spectroscopy at low temperatures (Fig. 4). In the previous report, we measured

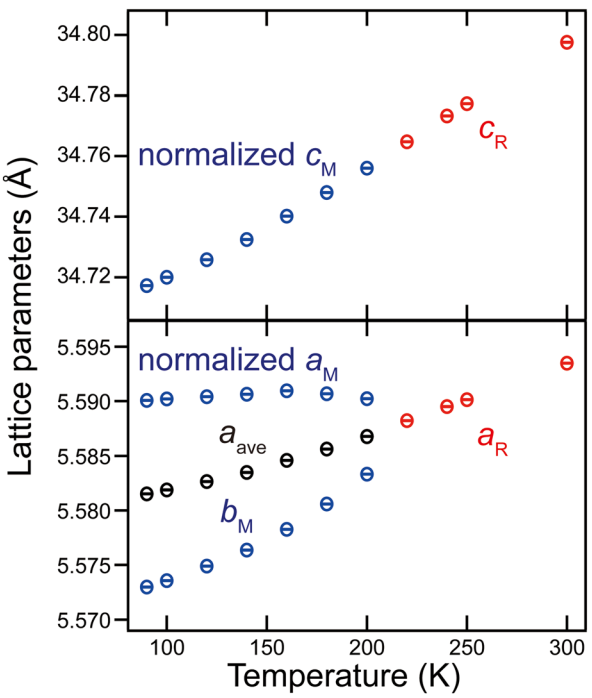

Fig. 2 Temperature dependence of lattice parameters of $SrV_{0.3}Fe_{0.7}O_{2.8}$. Here, a_{ave} represents the geometric mean of b_M and normalized a_M.

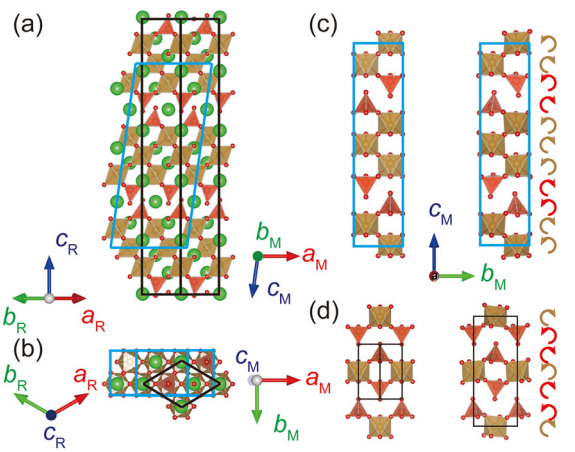

Fig. 3 (a and b) The transformation from $R\bar{3}m$ (black) to $C2/c$ (light blue) in $SrV_{0.3}Fe_{0.7}O_{2.8}$. (c) Octahedral tilting of $SrV_{0.3}Fe_{0.7}O_{2.8}$. Left is the high temperature phase without polyhedral tilting and right is the low temperature phase with polyhedral tilting. (d) Octahedral tilting of $Na_2BaFeV_2O_8$ at high (left) and low (right) temperatures.

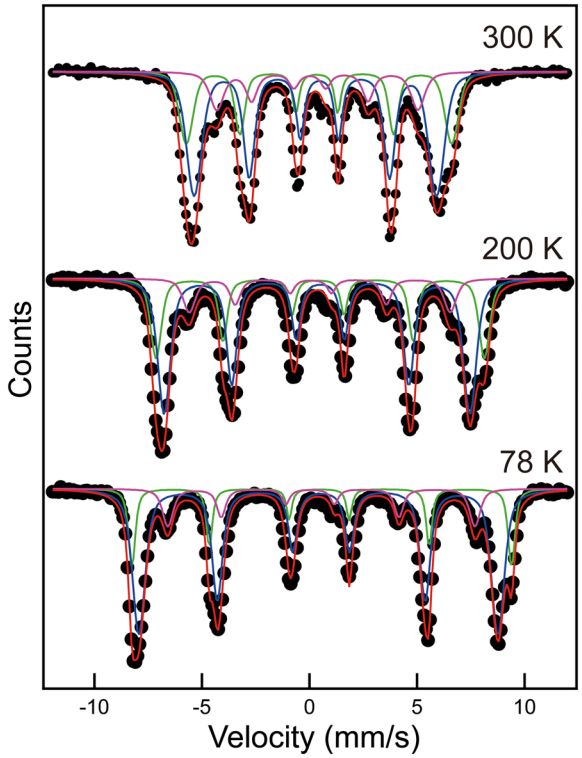

Fig. 4 ^{57}Fe Mössbauer spectra for $SrV_{0.3}Fe_{0.7}O_{2.8}$ taken at 78 K, 200 K, and 300 K. The spectrum at 300 K is taken from a previous study.[9] Black closed circles and lines represent the observed and calculated intensities. The green, blue, and pink lines represent subspectra from Fe1, Fe2, and Fe3, respectively. The red line represents the total fitted spectrum.

the ^{57}Fe Mössbauer spectrum for $SrV_{0.3}Fe_{0.7}O_{2.8}$ at 300 K, and three sets of subspectra were assigned to Fe1, Fe2, and Fe3 sites in the crystal structure.[9] Increased splitting width at low temperatures suggests an increase in the magnetic moments. Notably, the observed spectra also consist of three sets of sextet peaks even well below T_s, at 78 K. This means that there is no further site separation at each Fe site, consistent with the $C2/c$ structural model. Monotonous increase in the isomer shift (IS) and the almost constant quadrupole shift (QS) at Fe1 and Fe2 suggest that no significant deformation of the octahedra occurs (Table 1). In contrast, the increase of the QS at Fe3 at low temperatures indicates a significant change of local structure around the tetrahedra, which is also indicated by the shift of the Sr1 site from the result of the structural refinement. Overall, the ^{57}Fe Mössbauer spectra are consistent with the results of the structural analysis. Thus, the distorted structure of $SrV_{0.3}Fe_{0.7}O_{2.8}$ below T_s is caused by the polyhedral tilting along the a_M-axis.

Table 1 Isomer shift (IS), quadrupole shift (QS), and hyperfine field (HF) fitted from Mössbauer spectra on $SrV_{0.3}Fe_{0.7}O_{2.8}$ at 300 K, 200 K, and 78 K

	Site	IS (mm s^{-1})	QS (mm s^{-1})	HF (T)
300 K	Fe1	0.39	0.10	38.3
	Fe2	0.36	−0.19	34.9
	Fe3	0.19	0.35	29.0
200 K	Fe1	0.45	0.10	47.4
	Fe2	0.42	−0.16	44.1
	Fe3	0.26	0.41	37.6
78 K	Fe1	0.51	0.11	54.7
	Fe2	0.47	−0.13	51.8
	Fe3	0.29	0.52	44.3

We investigated the effects of structural phase transition on the physical properties. Fig. 5a shows field cool (FC) and zero field cool (ZFC) at 0.1 T (its derivative is shown in Fig. S6†). The anomaly can be observed at 200 K, corresponding to T_s. Around T_s, the shape of magnetization curves clearly changes (Fig. 5b). Although the coercivity (hysteresis) is almost zero above T_s, it prominently increases as temperature decreases below T_s. This is consistent with the discrepancy (hysteresis) between FC and ZFC becoming prominent below T_s. Namely, it can be assigned to the soft-to-hard ferrite transition.

The magnetic structure analysis shows that the low temperature phase also has antiferromagnetic component in the *ab* plane as the high temperature phase (Fig. S7†). Thus, the magnetic phase below T_s is also weak ferromagnetism based on the G-type antiferromagnetic order. Considering the determined magnetic structure and polyhedral tilting, we deduce that the change of magnetic behaviours originates from the change in magnetic anisotropy.

Temperature dependence of resistivity at 0 T, 1 T, 3 T, and 9 T are shown in Fig. 5c. Semiconductor-like behaviour and the decrease of resistance in the magnetic field are observed in the entire measurement range. In contrast to the magnetization, no anomaly at T_s is observed in the resistivity. We converted the resistance into the MR at each temperature (Fig. 5d). At 300 K, MR is proportional to the square of magnetization, indicating the tunnelling mechanism, as reported previously.[9] However, this relationship is broken below 300 K: the shape of MR becomes broader than that of magnetization (Fig. S8†). The MR increases as temperature decreases and reaches *ca.* −18% at 130 K and 9 T. This value is comparable to the magnetoresistance reported for other iron-base oxides ($Zn_{0.2}Ni_{0.8}Fe_2O_4$: *ca.* −20% at 150 K and 9 T (ref. 20)). Thus, $SrV_{0.3}Fe_{0.7}O_{2.8}$ can potentially exceed these values by chemical substitution to tune its physical properties.

Conclusions

In summary, we observed the structural phase transition from the rhombohedral to monoclinic phase caused by the polyhedral tilting in $SrV_{0.3}Fe_{0.7}O_{2.8}$ at 200 K. This phase transition affects the magnetic properties: the hysteresis becomes open and coercivity increases from almost zero as the temperature decreases. In addition, magnetoresistance increases as the temperature decreases, reaching *ca.* −18% at 130 K at 9 T. This material has the potential to show further large magnetoresistance by chemical substation.

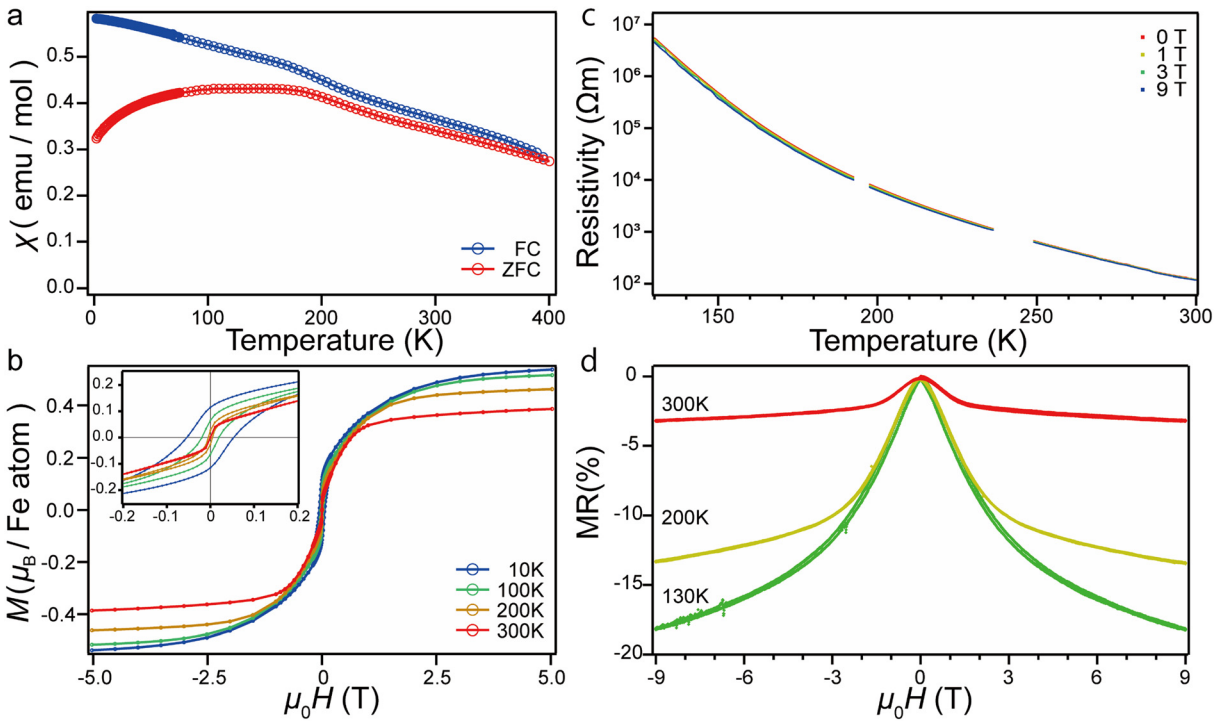

Fig. 5 FC-ZFC curves at 0.1 T (a) and *M*–*H* curves at 10, 100, 200, and 300 K (b) for $SrV_{0.3}Fe_{0.7}O_{2.8}$. The inset in Fig. 5b is an expansion near the zero-feild region. The *M*–*H* curve at 300 K is taken from the previous study.[9] (c) Temperature dependence of resistivity. (d) Magnetoresistance at 300, 200, and 130 K.

Data availability

The data supporting this article have been included as part of the ESI.†

Author contributions

T. Nagase and T. Y. designed the research. T. Nagase performed synthesis and characterization. T. Nagase, T. Nishikubo, Y. S., and K. S. performed physical measurements and K. M. performed and analyzed Mössbauer spectroscopy. M. H. performed neutron diffraction measurements. M. A. aided in the analysis of data. All the authors discussed the results. T. Nagase and T. Y. wrote the manuscript, with comments from all the authors.

Conflicts of interest

There are no conflicts to declare.

Acknowledgements

This work was supported by JSPS KAKENHI Grant Number JP22H01767. This work was also supported by the Design and Engineering by the Joint Inverse Innovation for Materials Architecture (DEJI2MA), MEXT. This work was supported by JST SPRING, Grant Number JPMJSP2106. Teppei Nagase was supported by the Japan Society for the Promotion of Science for Young Scientists (JP24KJ1052). The synchrotron radiation experiments were performed at the BL02B2 of SPring-8 with the approval of the Japan Synchrotron Radiation Research Institute (JASRI) (Proposal No. 2020A1068, 2024A1801). The neutron diffraction experiment was performed at the SuperHRPD diffractometer of J-PARC, MLF, with the approval of the Institute of Materials Structure Science (Proposal No. 2019S05). The Mössbauer spectroscopic study was supported by the Advanced Research Infrastructure for Materials and Nanotechnology (ARIM) Program of MEXT, Japan.

Notes and references

1 J. P. Hodges, S. Short, J. D. Jorgensen, X. Xiong, B. Dabrowski, S. M. Mini and C. W. Kimball, *J. Solid State Chem.*, 2000, **151**, 190–209.
2 L. Suescun, O. Chmaissem, J. Mais, B. Dabrowski and J. D. Jorgensen, *J. Solid State Chem.*, 2007, **180**, 1698–1707.
3 O. H. Hansteen, H. Fjellvåg and B. C. Hauback, *J. Mater. Chem.*, 1998, **8**, 2081–2088.
4 C. Greaves, A. J. Jacobson, B. C. Tofield and B. E. F. Fender, *Acta Crystallogr.*, 1975, **31**, 641–646.
5 J. Berggren, O. Foss, I. Roti, H. Okinaka, K. Kosuge and S. Kachi, *Acta Chem. Scand.*, 1971, **25**, 3616–3624.
6 M. Azuma, Z. Hiroi, M. Takano, Y. Bando and Y. Takeda, *Nature*, 1992, **356**, 775–776.
7 Y. Tsujimoto, C. Tassel, N. Hayashi, T. Watanabe, H. Kageyama, K. Yoshimura, M. Takano, M. Ceretti, C. Ritter and W. Paulus, *Nature*, 2007, **450**, 1062–1065.

8 T. Yamamoto, A. Chikamatsu, S. Kitagawa, N. Izumo, S. Yamashita, H. Takatsu, M. Ochi, T. Maruyama, M. Namba, W. Sun, T. Nakashima, F. Takeiri, K. Fujii, M. Yashima, Y. Sugisawa, M. Sano, Y. Hirose, D. Sekiba, C. M. Brown, T. Honda, K. Ikeda, T. Otomo, K. Kuroki, K. Ishida, T. Mori, K. Kimoto, T. Hasegawa and H. Kageyama, *Nat. Commun.*, 2020, **11**, 5923.

9 T. Nagase, T. Nishikubo, M. Fukuda, Y. Sakai, K. Shigematsu, Y. Ikeda, Y. Nambu, Q. Zhang, M. Matsuda, K. Mibu, M. Azuma and T. Yamamoto, *Inorg. Chem.*, 2022, **61**, 8987–8991.

10 A. M. Arévalo-López, F. Sher, J. Farnham, A. J. Watson and J. P. Attfield, *Chem. Mater.*, 2013, **25**, 2346–2351.

11 A. M. Arévalo-Lõpez, J. A. Rodgers, M. S. Senn, F. Sher, J. Farnham, W. Gibbs and J. P. Attfield, *Angew. Chem., Int. Ed.*, 2012, **51**, 10791–10794.

12 K. Momma and F. Izumi, *J. Appl. Crystallogr.*, 2011, **44**, 1272–1276.

13 V. Petrícek, M. Dušek and L. Palatinus, *Z. Kristallogr.*, 2014, **229**, 345–352.

14 B. J. Campbell, H. T. Stokes, D. E. Tanner and D. M. Hatch, *J. Appl. Crystallogr.*, 2006, **39**, 607–614.

15 Y. Han, X. Ye, H. Zhu, Y. Li and X. Kuang, *J. Solid State Chem.*, 2017, **247**, 20–23.

16 T. Yamamoto, Y. Otsubo, T. Nagase, T. Kosuge and M. Azuma, *Inorg. Chem.*, 2024, **63**, 4482–4486.

17 L. D. Sanjeewa, V. O. Garlea, M. A. McGuire, M. Frontzek, C. D. McMillen, K. Fulle and J. W. Kolis, *Inorg. Chem.*, 2017, **56**, 14842–14849.

18 A. Reuß, V. Ksenofontov, J. Tapp, D. Wulferding, P. Lemmens, M. Panthöfer and A. Möller, *Inorg. Chem.*, 2018, **57**, 6300–6308.

19 L. D. Sanjeewa, V. O. Garlea, M. A. McGuire, C. D. McMillen and J. W. Kolis, *Inorg. Chem.*, 2019, **58**, 2813–2821.

20 A. K. M. A. Hossain, M. Seki, T. Kawai and H. Tabata, *J. Appl. Phys.*, 2004, **96**, 1273–1275.

